



## LJMU Research Online

Murrell, GG and Baldry, IK

**Star formation rate density as a function of galaxy mass at  $z < 0.2$  with MUSE and GAMA surveys**

<https://researchonline.ljmu.ac.uk/id/eprint/26362/>

### Article

**Citation** (please note it is advisable to refer to the publisher's version if you intend to cite from this work)

**Murrell, GG and Baldry, IK (2025) Star formation rate density as a function of galaxy mass at  $z < 0.2$  with MUSE and GAMA surveys. Monthly Notices of the Royal Astronomical Society, 539 (3). pp. 1944-1954. ISSN 0035-8711**

LJMU has developed [LJMU Research Online](#) for users to access the research output of the University more effectively. Copyright © and Moral Rights for the papers on this site are retained by the individual authors and/or other copyright owners. Users may download and/or print one copy of any article(s) in LJMU Research Online to facilitate their private study or for non-commercial research. You may not engage in further distribution of the material or use it for any profit-making activities or any commercial gain.

The version presented here may differ from the published version or from the version of the record. Please see the repository URL above for details on accessing the published version and note that access may require a subscription.

For more information please contact [researchonline@ljmu.ac.uk](mailto:researchonline@ljmu.ac.uk)

# Star formation rate density as a function of galaxy mass at $z < 0.2$ with MUSE and GAMA surveys

Gregory G. Murrell<sup>★</sup> and I. K. Baldry<sup>Ⓜ</sup>

*Astrophysics Research Institute, Liverpool John Moores University, 146 Brownlow Hill, Liverpool L3 5RF, UK*

Accepted 2025 March 30. Received 2025 March 27; in original form 2024 October 4

## ABSTRACT

The star formation rate density (SFRD) is an important tool in galaxy evolution that allows us to identify at which cosmic time galaxies are more efficient at forming stars. For low-mass star-forming galaxies, the SFRD as a function of stellar mass can be straightforwardly related to the galaxy stellar mass function (GSMF). Given the uncertainty of the GSMF at the low-mass end, due to the challenges in observing dwarf galaxies, deriving the SFRD with respect to mass may be crucial to understand galaxy formation. Measurement of SFRD is more complete than number density in a cosmological volume because galaxies with higher star formation rate (SFR) are easier to detect and characterize. In this work, the SFRD is derived using two different samples, one using the MUSE Wide and MUSE Hubble Ultra-Deep Field integral-field unit spectroscopic surveys, and another using the Galaxy and Mass Assembly spectroscopic survey. The first sample comprised a total of 27 star-forming galaxies at  $z < 0.2$  ( $H\alpha$  selected), whereas the second contained 7579 galaxies at  $z < 0.06$  ( $r$ -band selected). The SFRs are derived from measurements of the  $H\alpha$  emission line fluxes for the first sample, and using MagPhys SED fitting for the second one. The results show the behaviour of the SFRD to the lowest stellar masses of  $10^{5.5} M_{\odot}$ , consistent with a constant slope (in log SFRD versus log stellar mass) and thus no turn-over in the GSMF.

**Key words:** galaxies: luminosity function, mass function.

## 1 INTRODUCTION

The star formation rate density (SFRD) is defined as the total star formation rate (SFR) averaged over a given comoving volume of the Universe observed at a given redshift (Madau et al. 1996). Understanding the evolution of the SFRD across cosmic history may unravel crucial insights into how galaxies grow and evolve, constraining cosmological models (Schaye et al. 2010). When measuring its contribution as a function of redshift, it allows us to understand at which cosmic time, star formation is more favourable in galaxies; whereas if analysed with respect to galaxy stellar mass, the SFRD may provide useful information on the role of galaxy mass in star formation (Gilbank et al. 2010b).

SFRD measurements over cosmic time have become a common practice in modern astrophysics in the past three decades. Numerous studies have estimated the shape of SFRD, with literature agreeing that it peaks at around  $z \sim 2-3$ , declines in more recent epochs, with another sharper drop at  $z > 8$  (Bouwens et al. 2015). Lilly et al. (1996) pioneered the analysis of SFRD, conducting the first systematic work to combine a large and deep spectroscopic redshift survey with multiwavelength photometry, and deriving the luminosity function and SFRD to redshifts of  $z \sim 1$ . Hopkins & Beacom (2006) showed how the cosmic star formation history may be disclosed by measurements of the SFRD, as it shows in which epochs star formation is more favourable. Hubble Space Telescope (HST) data was used by Bouwens et al. (2015) to push the limits

of SFRD to the highest redshifts, as they derived the SFRD from ultraviolet (UV) luminosity functions to redshifts of  $z \sim 10$ , showing a sharp decrease in star formation at redshifts of  $z > 8$ . Madau & Dickinson (2014) reviewed over 200 SFRD measurements from the literature, reporting methodologies and results, alongside connecting the observational results with cosmological theories.

Although there has been a vast number of studies on how SFRD evolves over time, the same cannot be said on how SFRD relates to other intrinsic galaxy properties. Understanding the relation between SFRD and other physical properties may give us additional information on how galaxies evolve and assemble (Madau & Dickinson 2014). For example, James et al. (2008a) have shown that SFRD varies significantly with galaxy morphology, highlighting the importance of galaxy type in shaping star formation activity. Schulze et al. (2021) measured core-collapse supernovae (CCSNe) rates (closely related to SFRD) as a function of galaxy mass for different types of supernovae. If analysed with respect to mass distribution, the SFRD provides useful insights of how galaxies of given masses contribute to the total SFR budget across cosmic time, revealing mass-dependent trends in star formation history (Gilbank et al. 2010a; Khostovan et al. 2024). Studies such as Drake et al. (2015) have further examined this relation, showing how star formation evolves with stellar mass between redshifts  $z = 1.46$  and  $z = 0.63$ .

For low-mass star-forming galaxies, assuming that the mean specific SFR is approximately constant for masses smaller than  $\sim 10^9 M_{\odot}$ , measurements of the SFRD can give an estimate of the galaxy stellar mass function (GSMF; Sedgwick et al. 2019). This assumption is confirmed by the analysis of  $H\alpha$  emission as a function of galaxy stellar mass (James, Prescott & Baldry 2008b)

<sup>★</sup> E-mail: [G.G.Murrell@2021.ljmu.ac.uk](mailto:G.G.Murrell@2021.ljmu.ac.uk)

and by unquenched low-mass galaxies, dwarf galaxies whose cold gas reservoir has not been emptied by any physical mechanism, as they have been forming stars at a quasi-constant rate, meaning that it is reasonable to expect that their *mean* specific SFR is  $\sim 10^{-10} \text{ yr}^{-1}$  (van Zee 2001).

Gilbank et al. (2010b) calculated the SFRD using  $H\alpha$ ,  $[O II]$ , and  $u$ -band luminosities from the Sloan Digital Sky Survey (SDSS; York et al. 2000) coupled with UV data from the Galaxy Evolution EXplorer (GALEX) satellite (Budavári et al. 2009), deriving the SFRD with respect to stellar mass down to masses of  $\sim 10^8 M_\odot$ . However, the derivation of the SFRD at lower masses has proven to be a challenge due to the extremely low surface brightness of dwarf galaxies (Cross & Driver 2002). Sedgwick et al. (2019) introduced a novel approach, using CCSNe as ‘signposts’ to low surface brightness galaxies to constrain their abundance and contribution to the total SFRD at lower masses. Rates are converted to SFRDs using the expected CCSNe per unit mass of star formation. The work from Sedgwick et al. (2019) suggests that a greater fraction of star formation occurs in low-mass, low surface brightness galaxies than previously thought. Nevertheless, more sensitive surveys are needed to fully capture the star formation activity and extend SFRD measurements to smaller and fainter systems.

Previous studies of SFRD have used emission lines and broad-band photometric tracers to extend SFRD measurements to low stellar masses across cosmic time, with the  $H\alpha$  emission line being one of the best indicators of star formation in a galaxy, since young, massive stars with ages  $< 20$  Myr produce copious amounts of ionizing photons that ionize the surrounding gas (Davies et al. 2016). This is a great advantage when calculating the SFR of a galaxy, as only young stars are taken into account and thus it is largely independent of star formation history (Kennicutt 1998). Additionally, compared to other emission lines,  $H\alpha$  is the most directly proportional to the ionizing UV stellar spectra at  $\lambda < 912 \text{ \AA}$  and it is not as susceptible to the metal fraction present in the gas (Tresse & Maddox 1998). A limitation of using  $H\alpha$  as an SFR indicator is that the aperture-based spectroscopy only probes the central regions of nearby galaxies (Davies et al. 2016), but this can be corrected with the appropriate calibration or with integral-field unit (IFU) spectroscopy.

As modern IFU surveys can provide complete spatial and spectral coverage, detecting emission lines even for the faintest and most diffuse sources that lack continuum, they can be used to probe the faintest galaxy populations, extending SFRD measurements to the lowest masses (Bacon et al. 2015; Herenz et al. 2017). The MUSE Hubble Ultra-Deep Field (HUDF; Bacon et al. 2023) and MUSE Wide (Urrutia et al. 2019) are optical IFU spectroscopic surveys from the Multi-Unit Spectroscopic Explorer (MUSE) collaboration that can reach unprecedented depths compared to similar spectroscopic surveys.

In this work, the low-mass galaxy population at redshift  $\leq 0.2$  is characterized using MUSE Wide and MUSE HUDF, deriving their SFRs through the analysis of their  $H\alpha$  emission line fluxes. Using this information, the SFRD with respect to stellar mass of the population for the combined MUSE sample is calculated. The SFRD is also derived using the Galaxy and Mass Assembly (GAMA) survey. GAMA is a much larger spectroscopic survey but is selected using broad-band SDSS photometry and is expected to be significantly incomplete to low surface brightness galaxies below about  $10^8 M_\odot$  (Baldry et al. 2012). Results of both approaches are presented to determine the contribution of the low-mass galaxy population to the cosmic SFRD.

A description of the data sets used is presented in Section 2, the principles of the SFRD measurements are presented in Section 3,

sample selection and processing in Section 4, and the main results in Section 5; with discussion and summary in the final sections. An  $\Omega_m = 0.3$  flat- $\Lambda$  cosmology with  $H_0 = 70$  is assumed for distances and volumes.

## 2 DATA SAMPLE AND SURVEYS DESCRIPTION

In this section, we describe the source data and the different surveys used in this study. Each subsection details the characteristics of the each survey, explaining the data release used, how the measurements were derived, and which catalogues are used in this study.

### 2.1 MUSE Wide

The MUSE Wide survey is a large spectroscopic survey that uses the MUSE instrument on the Very Large Telescope to observe galaxies in the distant universe (Bacon et al. 2010). The MUSE Wide survey is a blind, 3D spectroscopic survey that provides, like many other extragalactic surveys, a ‘wedding-cake’ approach, and is expected to cover  $100 \times 1$  arcmin<sup>2</sup> MUSE fields by the end of the survey (Urrutia et al. 2019). MUSE Wide mainly covers parts of the Chandra Deep Field South (CDFs) and the Cosmological Evolution Survey (COSMOS) regions that were previously mapped by HST in several bands to intermediate depths, by the Great Observatories Origins Deep Survey (GOODS)-South in the optical (Giavalisco et al. 2004) and by the Cosmic Assembly Near-infrared Deep Extragalactic Legacy Survey (CANDELS) in the near infrared (Grogin et al. 2011; Koekemoer et al. 2011). The survey is designed to cover the whole field of view continuously, so that it is not restricted to a photometric pre-selection for identification and classification of objects in the sky (Bacon et al. 2017).

The first data release (DR1) consists of 44 CANDELS-CDFS fields, with observations carried out in nominal mode (each spectrum spans from 4750 to 9350  $\text{\AA}$  in wavelength range), and  $0.2 \text{ arcsec} \times 0.2 \text{ arcsec}$  spatial and 1.25  $\text{\AA}$  wavelength sampling, which is the default for MUSE (Urrutia et al. 2019). The survey used a combination of spectroscopic and photometric measurements to derive the stellar masses of the galaxies in their catalogue. The photometry was taken from Skelton et al. (2014), while the software FAST (Fitting and Assessment of Synthetic Templates; Kriek et al. 2018) was used for the spectral energy distribution (SED) fitting model. FAST determines the best-fitting parameters using  $\chi^2$  minimization from a set of model SEDs and an analysis grid describing several stellar population models.

The catalogues used in this study were retrieved from the MUSE Wide DR1 data base, which is available on their website (MUSEWIDE\_DR1). The two catalogues used in this work MUSE, one being the MUSE Wide main table (musewide\_dr1.mw\_44fields\_main\_table), from which the columns containing galaxy properties such as redshift and stellar mass, and their associated source with the Skelton et al. (2014) catalogue, were extracted (columns names respectively: Z, STELLAR\_MASS, SKELTON\_ID, SKELTON\_SEP). The other catalogue used is the MUSE Wide emission line table (musewide\_dr1.mw\_44fields\_emline\_table), containing information about line fluxes at different Kron radius apertures (column used F\_2KRON, which comprises values for emission line fluxes extracted in an aperture equivalent to Kron radius  $\times 2$ ). The emission line and source identification was performed using LSDCAT (Herenz & Wisotzki 2017), an automated detection package for emission lines in wide-field integral-field spectroscopic datacubes. The full description of the data release and catalogues

is reported in the documentation from Urrutia et al. (2019) and Herenz & Wisotzki (2017).

## 2.2 MUSE Hubble Ultra-Deep Field

The MUSE HUDF survey is a deep spectroscopic survey of the HUDF region. The second data release (DR2) provides the deepest IFU spectroscopic survey to date, alongside excellent 3D content, wide spectral range, and outstanding spatial and spectral resolution (Bacon et al. 2023). The survey is based on three MUSE data sets at various depths: MOSAIC ( $3 \times 3$  arcmin<sup>2</sup>, 10 h), UDF-10 (1 arcmin<sup>2</sup>, 31 h), and MUSE eXtremely Deep Field (MXDF). The stellar masses of the galaxy sample of the survey were derived using SED fitting. In order to perform the SED fit with sufficient constraints, photometry from the HST R15 (Rafelski et al. 2015) catalogue was used, as the catalogue contains 11 photometric bands ranging from the NUV (0.21  $\mu$ m) to the WFC3/IR (1.5  $\mu$ m). The stellar masses were calculated using two different SED fitting codes: the high- $z$  extension of MagPhys (da Cunha, Charlot & Elbaz 2008; da Cunha et al. 2015), with minimum stellar mass of  $10^6 M_{\odot}$ , and Prospector (Johnson et al. 2021). However, it is reported that Prospector tends to derive higher values for stellar masses compared to MagPhys, with a median offset of 0.25 dex, which is a known characteristic of Prospector (Leja et al. 2020).

From the MUSE HUDF survey, the data from the DR2 main table (dr2\_main\_09) is used for the analysis. The table contains galaxy properties like redshift and stellar mass derived using MagPhys, which can be accessed via their respective columns ‘Z’ and ‘MASS\_MAG’. For each galaxy, the table also contains values for emission line fluxes, with the  $H\alpha$  flux values used being stored in the ‘HALPHA\_EMI\_FLUX’ column. For the MUSE HUDF survey, the source detection and classification was performed using the blind detection software ORIGIN, capable of detecting faint line emitters in MUSE datacubes (Mary et al. 2020). The data set is publicly available and may be retrieved from the collaboration website (MUSEHUDF\_DR2). For full description of the survey and catalogues, please refer to Bacon et al. (2023).

## 2.3 GAMA

The GAMA survey (Liske et al. 2015; Baldry et al. 2018; Driver et al. 2022) is a spectroscopic redshift and multiwavelength photometric survey designed to study galaxy evolution. The survey is divided into five regions: three equatorial regions (G09, G12, G15) each of 60.0 deg<sup>2</sup> and main survey limit of  $r_{AB} < 19.8$  mag, and two southern regions of 55.7 deg<sup>2</sup> (G02) and 50.6 deg<sup>2</sup> (G23). Here, we use the equatorial regions, which cover an area of 179 deg<sup>2</sup> after accounting for masking around bright stars.

The fourth data release of GAMA (DR4) is the final release (Driver et al. 2022). Compared to MUSE Wide and MUSE HUDF, GAMA is shallower. Moreover, it relies on fibre spectroscopy, which may result in an overestimation of emission line fluxes and SFRs for small or low surface brightness galaxies when applying aperture corrections (Richards et al. 2016). However, GAMA benefits from a much wider area and larger catalogue, comprising 21-band photometric data with spectroscopic line emission measurements for star formation indicators O II and  $H\alpha$ , containing information for stellar mass estimates of 198 223 galaxies, and measured redshifts for 196 402.

The survey data is organized into data management units (DMUs). The DMUs used in this work are SpecCat, containing the spectra and redshifts from all the curated spectroscopic data of the GAMA survey, with the primary choice of redshift extracted using the automatic

code AUTOZ (Baldry et al. 2014); StellarMasses, which provides measurements of the total stellar mass of the sources (Taylor et al. 2011); and MagPhys (da Cunha et al. 2008) that contains estimates of a number of key parameters including stellar mass, dust mass, and SFR (Driver et al. 2018). For the descriptions of other DMUs, please refer to Baldry et al. (2018) and Driver et al. (2022). Note that we prefer the MagPhys estimates of the SFRs compared to the  $H\alpha$  fluxes (Hopkins et al. 2013; Gordon et al. 2016) because, in the latter case, the fluxes are indirectly derived from equivalent widths and  $r$ -band photometry which can result in unverified high SFR outliers (Davies et al. 2016) that significantly impact SFRD measurements.

## 3 DERIVATION OF THE STAR FORMATION RATE DENSITY WITH THE $1/V_{\max}$ METHOD

### 3.1 Star formation rate from $H\alpha$ emission lines

Star-forming galaxies produce very specific emission lines in their spectra that can be easily characterized.  $H\alpha$  emission lines are one of the best indicators for star-forming galaxies, since only young, massive stars with ages  $< 20$  Myr produce vast amounts of photons that ionize the surrounding gas (Davies et al. 2016). This is a great advantage when calculating the SFR of a galaxy, as only young stars are taken into account and thus it is largely independent of star formation history (Kennicutt 1998). Assuming a Kroupa initial mass function (Kroupa 2001), the relation between the  $H\alpha$  luminosity and SFR may be obtained with the following calibration (Calzetti 2013):

$$\text{SFR}_{H\alpha} = 5.5 \times 10^{-42} L(H\alpha), \quad (1)$$

with  $\text{SFR}(H\alpha)$  in  $M_{\odot} \text{ yr}^{-1}$  and  $L(H\alpha)$  in  $\text{erg s}^{-1}$ . The calibration constant is valid provided that star formation has remained constant over time-scales  $> 6$  Myr, with no dependence on long time-scales (Calzetti 2013). This calibration does not take into account active galactic nucleus (AGN) contamination, which could theoretically result in an overestimation of  $\text{SFR}(H\alpha)$ . However, for low-mass galaxies AGN contamination is not a significant issue (Kauffmann et al. 2003).

### 3.2 Star formation rate density with the $1/V_{\max}$ method

The SFRD with respect to mass can be calculated using the  $1/V_{\max}$  method. The  $1/V_{\max}$  method (Felten 1976) corrects for survey biases by weighting galaxies according to the maximum comoving volume in which they could be detected. This ensures that fainter galaxies, observable over smaller volumes, contribute proportionately more to the overall density estimate. The comoving volume may be derived using the following equation:

$$V_{\max} = \frac{\Omega}{3} (D_{\max}^3 - D_{\min}^3), \quad (2)$$

where  $\Omega$  is the solid angle of the field of view (FOV) of the survey, and  $D_{\max}^3$  and  $D_{\min}^3$  are the maximum and minimum comoving distance for which the object could be observed given its luminosity and considering the survey limits. Note for a redshift-limited sample, the brighter sources that are limited only by the redshift range will have the same  $V_{\max}$ .

If more than one survey is used, the  $V_{\max}$  estimate has to consider the total volume of the surveys. This can be done assuming that a source may be observed at any given point of the surveys. Therefore, if two surveys are used, the total  $V_{\max}$  may be calculated by adding the  $V_{\max}$  of a galaxy in each survey:

$$V_{\text{tot}} = V_{\max,1} + V_{\max,2}, \quad (3)$$

with  $V_{\max,1}$  being the comoving volume of the source in its ‘parent’ survey, and  $V_{\max,2}$  the comoving volume if the galaxy had been observed in the other survey.

Once the total comoving volume has been defined, the  $1/V_{\max}$  method may be used to derive the SFRD as a function of mass in the  $m$ th bin using the following relation:

$$\rho_{\text{SFR},m} = \frac{1}{\Delta \log M} \sum \frac{\text{SFR}_i}{V_{\max,i}}, \quad (4)$$

where for the  $i$ th galaxy,  $\text{SFR}_i$  is its SFR,  $V_{\max,i}$  is its maximum volume from which the object could still be detected, and  $\Delta \log M$  is the bin width. In other words, this provides a binned estimate of  $\text{dSFRD}/\text{d} \log M$  in units of solar masses per year per  $\text{Mpc}^3$  per dex.

### 3.3 Estimation of $D_{\max}$

In order to correctly apply the  $1/V_{\max}$  method described in Section 3.2, it is necessary to estimate the maximum distance at which a source can be observed given its luminosity. This can be done in different ways. For the sample from MUSE Wide and MUSE HUDF,  $D_{\max}$  was derived by defining a minimum flux detection limit (see Section 4.2 for derivation). If the detection limit is defined as the minimum flux that a source must have in order to be included in the sample ( $F_{\text{lim}}$ ), one can work out the maximum luminosity distance ( $D_{L,\max}$ ) at which it can be observed by rearranging the relationship between bolometric luminosity and flux:

$$F_{\text{lim}} = \frac{L}{4\pi D_{L,\max}^2}. \quad (5)$$

In the case of bolometric flux, i.e. with no  $k$ -correction, then

$$D_{L,\max} = D_{L,\text{obs}} \sqrt{\frac{F_{\text{obs}}}{F_{\text{lim}}}}. \quad (6)$$

where  $F_{\text{obs}}$  is the observed flux and  $D_{L,\text{obs}}$  is the observed luminosity distance. This applies to line emission.

The  $D_{\max}$  values for the galaxies in the GAMA survey were derived using redshift and magnitude data from SDSS. The procedure requires calculating  $k$ -corrections, at a range of redshifts, in order to iterate towards an estimate for the maximum distance. The maximum distance can be obtained from the distance modulus given by

$$\text{DM}_{\max} = \text{DM}_{\text{obs}} + m_{\text{lim}} - m_{\text{obs}} + \text{d}K, \quad (7)$$

where  $\text{DM}_{\text{obs}}$  is the distance modulus at the observed redshift,  $m_{\text{lim}}$  is the magnitude limit of the survey,  $m_{\text{obs}}$  is the observed magnitude of the source, and  $\text{d}K$  is the differential  $K$ -correction. The latter is given by

$$\text{d}K = k_{\max,\text{obs}} + 2.5 \log(1 + z_{\max}), \quad (8)$$

where  $k_{\max,\text{obs}}$  is the  $k$ -correction of the observed galaxy for the effective band at  $z_{\max}$  (see Blanton et al. 2003 for this nomenclature). This is obtained by iterating: starting from  $\text{d}K = 0$  and determining a new  $\text{d}K$  by interpolation from a vector of band-shifted  $k$ -correction values on each iteration. Note that  $k_{\text{obs,obs}} = -2.5 \log(1 + z_{\text{obs}})$ , ensuring that  $\text{d}K$  converges to zero when  $z_{\max} = z_{\text{obs}}$ .

### 3.4 Dust extinction

In order to accurately measure the SFR, dust extinction corrections must be taken into account.  $\text{H}\alpha$  line is situated in the optical spectrum, making it less sensitive to dust extinction compared to other star formation indicators such as UV light. However, even

for local galaxies, dust effects on  $\text{H}\alpha$  are significant (Koyama et al. 2015). A common practice to determine the levels of dust attenuation in galaxies is to measure the ratio between  $\text{H}\alpha$  and  $\text{H}\beta$ , also known as the Balmer decrement. The theoretical value of the Balmer decrement, assuming that a optically thick star-forming region for all Lyman lines greater than  $\text{Ly}\alpha$ , is equal to 2.86 (Calzetti et al. 2000). Therefore, for a fixed electron temperature of  $10^4$  K, one can assume that any deviation from the theoretical value is due to dust extinction (Groves, Brinchmann & Walcher 2012).

The magnitude extinction  $A_V$  from the observed Balmer decrement may be calculated using the relation described in Osterbrock & Ferland (2006), with the  $E(B - V)$  colour excess that can be calculated directly from the Balmer decrement using the equation (see Domínguez et al. 2013):

$$E(B - V) = \frac{2.5}{k(\text{H}\beta) - k(\text{H}\alpha)} \times \log \left( \frac{(\text{H}\alpha/\text{H}\beta)_{\text{obs}}}{2.86} \right), \quad (9)$$

with the extinction coefficients  $k(\text{H}\alpha)$  and  $k(\text{H}\beta)$  coming from the reddening curve between  $\text{H}\alpha$  and  $\text{H}\beta$  described in Cardelli, Clayton & Mathis (1989). The dust correction factor is then derived with Calzetti et al. (2000):

$$\text{Dust correction factor} = 10^{0.4E(B-V)k(\text{H}\alpha)}. \quad (10)$$

Finally, the correction factor can be used to account dust extinction in the observed  $\text{H}\alpha$  flux:

$$\text{H}\alpha \text{ Flux}_{\text{corr}} = \text{H}\alpha \text{ Flux}_{\text{obs}} \times \text{dust correction factor}. \quad (11)$$

## 4 ANALYSIS

### 4.1 Sample selection

Initially, all the galaxies in the MUSE Wide and HUDF catalogues (Urrutia et al. 2019; Bacon et al. 2023) that presented  $\text{H}\alpha$  emission lines at redshift  $\leq 0.2$  were considered. Since the two areas covered by HUDF and Wide overlap slightly, it was also ensured that there were no duplicated galaxies, resulting in a preliminary sample of 21 star-forming galaxies from MUSE Wide emission line catalogue and 10 from MUSE HUDF main catalogue. In order to verify the accuracy of the redshift measurements, AUTOZ, which is a fully automated redshift code that allows us to homogenize redshift measurements (Baldry et al. 2014), was run over the entire area. The test resulted in no significant difference between the values reported in the MUSE Wide and HUDF catalogues, and the redshifts derived using AUTOZ.

MUSE Wide DR1 and MUSE HUDF DR2 used different photometry to derive the stellar masses values for the galaxies, the Skelton et al. (2014) and the HST R15 Rafelski et al. (2015) catalogues, respectively. The HST R15 Rafelski et al. (2015) catalogue used in HUDF does not contain values for  $F160W$  magnitude for all the sources in the catalogue. Therefore, photometry from the van der Wel et al. (2014) catalogue was used instead, as it contained values for all the sources in the sample. In order to ensure consistency, the photometric catalogues the  $F160W$  magnitudes were compared. This allowed us to assume that using photometric values from either catalogue does not affect the derivation of the  $H$ -band luminosity of the sources.

Using the  $F160W$  magnitude values from the van der Wel et al. (2014) catalogue, the  $H$ -band luminosities of all the galaxies in the sample were calculated. This information was then used to derive the stellar mass of two sources in the HUDF region that do not have a valid derivation for the stellar mass using MagPhys. In fact, Source ID6474 does not have a photometric value in R15, whereas

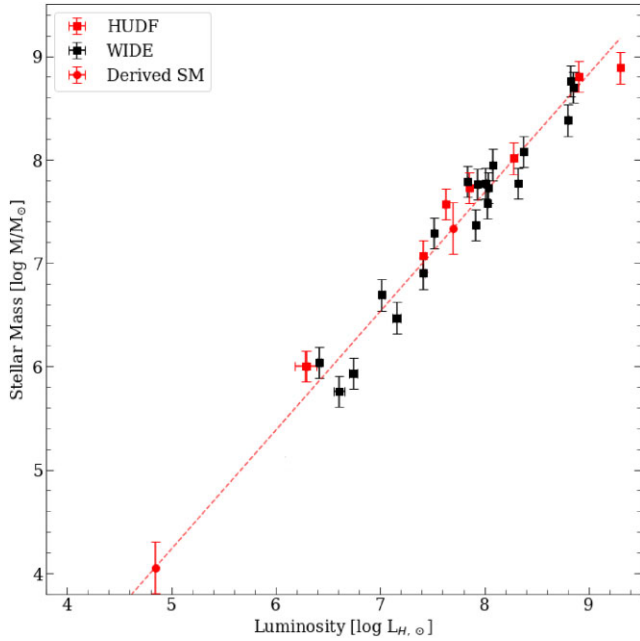


**Figure 1.** Mass–luminosity relation of the galaxies in the sample. The luminosities are derived using van der Wel et al. (2014) photometric catalogue. Using the log–log linear fit shown on this plot, the stellar masses of the sources without a valid mass on the catalogue were derived (these two sources are shown with circles on top of the line). An indicative stellar mass uncertainty was used. This was obtained by calculating the root-mean-square (RMS) difference between two different estimates from the MagPhys and Prospector codes.

the stellar mass of source ID8051 is likely extremely low. In order to include them in the sample, as they both present  $H\alpha$  emission lines, their stellar masses were derived using the typical stellar mass-to-luminosity ratio of star-forming galaxies.

The relation between stellar mass and luminosity of the sample is shown in the plot in Fig. 1, showing a linear relationship in the log–log scale. Hence, the stellar mass of the two star-forming galaxies was derived, with the assumption that they follow the stellar mass–luminosity relation.

The stellar masses of the sample can be seen in Fig. 2, where the values of the masses with respect to redshift are shown. ID8051, whose stellar mass was derived using the mass–luminosity relation, appears to have an exceptionally low mass of  $\sim 10^4 M_{\odot}$ , which, if confirmed to be accurate, would be one of the lowest stellar masses known of star-forming galaxies.

#### 4.2 Detection limit

Estimating the detection limits of the surveys is necessary in order to perform the  $1/V_{max}$  method (Schmidt 1968). In fact, because they affect the maximum volume within which objects can be detected, a failure to account for this bias can lead to incorrect estimates of the space density of the population being studied. However, the derivation of detection limits is often very complex, as there are many factors such as sky lines, atmospheric conditions, and aperture sizes that need to be considered.

In order to simplify the derivation of the detection limit and the calculation of  $V_{max}$ , an empirical detection limit (i.e. sample-selection limit) was set by analysing all the emission line fluxes detected in the survey between 6563 and 7876 Å, which is the region where  $H\alpha$  is expected to be found at  $z \leq 0.2$ . A reasonable assumption

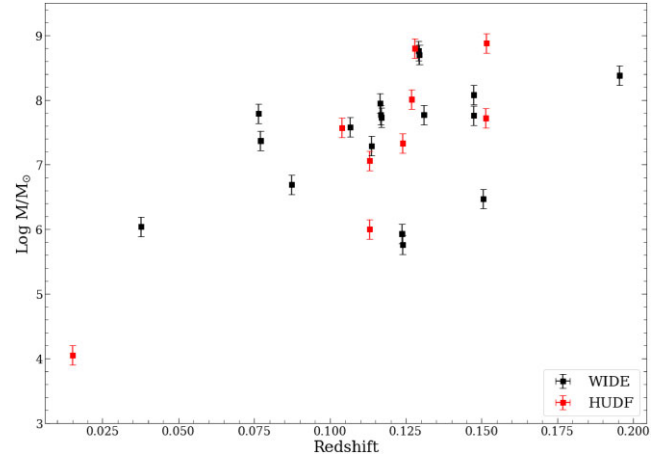


**Figure 2.** Stellar mass with respect to redshift for the combined sample of MUSE Wide emission line catalogue (Urrutia et al. 2019) and MUSE HUDF catalogue (Bacon et al. 2023). From the plot, it can be seen that the sample is comprised by very low mass star-forming galaxies, with all the galaxies with stellar masses below  $\sim 10^9 M_{\odot}$ . Please note that the plot also shows ID8051 (red square, lowest stellar mass in the sample) as its mass was derived using the stellar mass–luminosity relation, but it is not used in the calculation of the SFRD as it falls just below the empirical detection limit.

would be that the highest number of observations will have values just above the detection limit, and that below the limit there will be a sharp decrease in detections, since the instrument would have more difficulty in detecting the signal below a certain threshold.

Using the histogram shown in Fig. 3, the detection limit was estimated. It can be seen that there is a significant decline in number of emission lines observed right before the peak in the histogram. The detection limits were thus set to be the cut-off values where the number of detections dropped, which can be seen in the plots as the red dashed line. The plots also show all the emission line fluxes detected between 6563 and 7876 Å, with the red points representing the  $H\alpha$  lines. The results show that all the  $H\alpha$  emissions in MUSE Wide, and all but one in MUSE HUDF, are above the empirically estimated detection limits. The source below this limit (MUSE HUDF ID8061) is excluded from the estimation of the SFRD.

#### 4.3 Dust effects

Since  $H\alpha$  is affected by dust extinction in the optical range, it is essential to consider dust effects on emission line flux measurements in order to derive accurate SFR results. As described in Section 3.4, the most robust way to estimate dust extinction in a galaxy is by measuring the flux ratio between  $H\alpha$  and  $H\beta$ , also known as the Balmer decrement. One caveat of this method is that the  $H\beta$  line is often very faint and undetectable, particularly for smaller, fainter galaxies such as the sources in our sample. To overcome the absence of  $H\beta$  lines in our sample, the Balmer decrement for galaxies of similar properties was derived from the SDSS (York et al. 2000) and used to estimate the typical Balmer decrement of star-forming galaxies in a mass bin. This approach assumes that the median Balmer decrement trend with stellar mass also applies to the MUSE sample.

The total stellar mass of star-forming galaxies correlates with average metallicity, size, and dust mass (Beeston et al. 2018). So naturally, the dust extinction is lower in low-mass galaxies because less sightlines go through high extinction regions. Thus for our purposes, where we do not have individual Balmer decrement

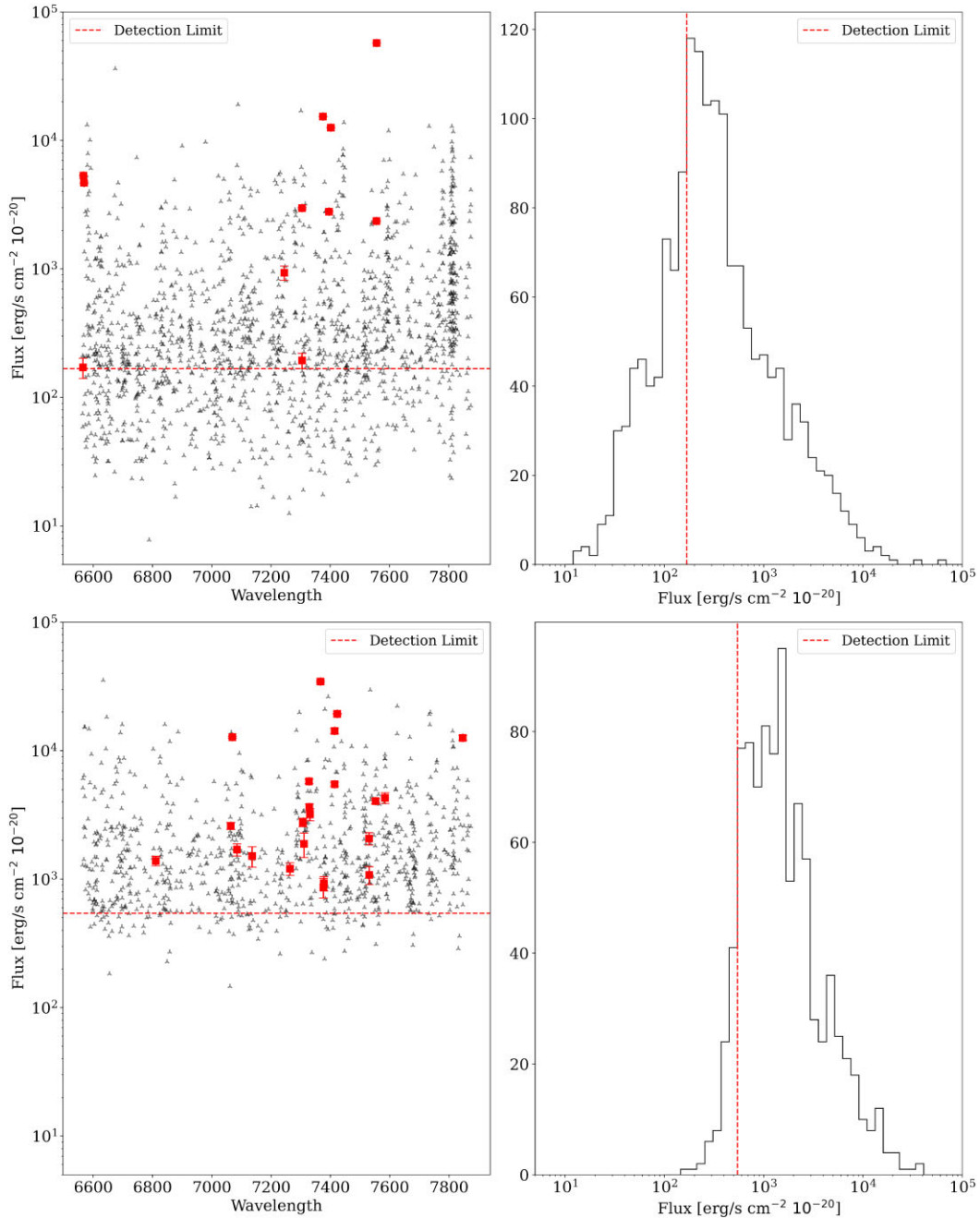


**Figure 3.** Derivation of the detection limit for the MUSE HUDF sample (top panels) and MUSE Wide sample (bottom panels). On the left panels, it is possible to visualize all the emission lines (grey triangles) detected in the range of interest, with the red squares indicating the detected  $H\alpha$  lines. It can be seen how MUSE HUDF is much deeper compared to MUSE Wide, as there are significantly more detections at lower fluxes. On the right panels, the histograms of the line fluxes are shown. The red dashed lines indicate the sample selection limits.

measurements, an average value as a function of stellar mass is the best estimate we can make.

From SDSS, all the galaxies with measured  $H\alpha$  and  $H\beta$  emission line fluxes (Brinchmann et al. 2004; Tremonti et al. 2004) and  $H\alpha$   $S/N > 20$  were considered. Then, the Balmer decrement for each galaxy was calculated, before determining the median value for each stellar mass bin of  $\Delta \log M = 0.5$ . From these points, a simple relation between Balmer decrement and stellar mass was derived using a quadratic function for stellar masses larger than  $10^{8.5} M_{\odot}$ , and assuming a constant decrement at lower masses. This provides

a robust estimate that is sufficient for the scope of this study. The results are reported in Fig. 4, where the red line shows the relation between Balmer decrement of star-forming galaxies and their stellar mass, where it is possible to see how galaxies with lower stellar masses are significantly less affected by dust. The resulting values for Balmer decrement and dust extinction for each mass bin are reported in Table 1.

This dust extinction–mass relation has been observed many times over the past decades, showing that the Balmer decrement, and thus dust extinction, is significantly larger in high-mass galaxies (Garn &

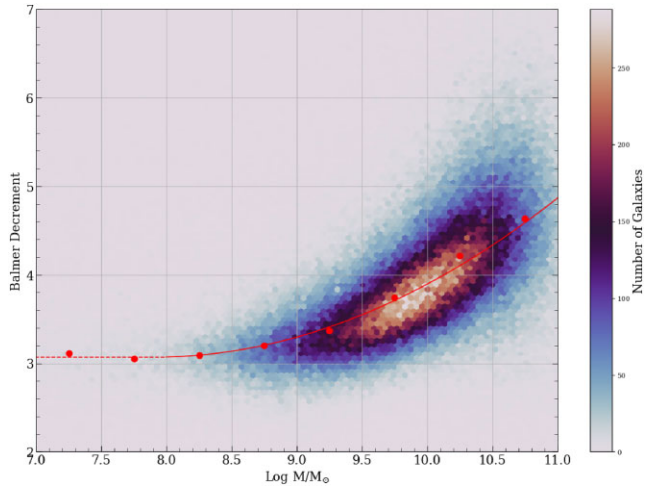


**Figure 4.** Balmer decrements derived using SDSS galaxies. The red solid line represents the median fit per each stellar mass bin of  $\Delta \log M = 0.5$ . The median fit was derived only for galaxies with stellar masses larger than  $10^{8.5} M_{\odot}$ , as there is a non-negligible scatter at lower masses. The dotted line is the constant value used for bins with stellar mass lower than  $10^8 M_{\odot}$ .

**Table 1.** Average Balmer decrements used in this study based on an analysis of SDSS star-forming galaxies and the dust correction factor.

Mass bin	Balmer decrement	Dust correction factor
<7.5	3.07	1.20
7.5–8.0	3.07	1.20
8.0–8.5	3.09	1.22
8.5–9.0	3.20	1.35
9.0–9.5	3.41	1.58

Best 2010; Domínguez et al. 2013). For low-mass galaxies, the accuracy of the SFRD is not limited by the dust extinction estimate (only a correction factor of 1.2), whereas for high-mass galaxies ( $> 10^{10} M_{\odot}$ ), it is arguably the limiting factor.

#### 4.4 $H\alpha$ luminosity function

In order to place the depth of the  $H\alpha$  selected sample into context, we compute the  $H\alpha$  luminosity function using the  $1/V_{\max}$  values for the combined MUSE sample. The observed  $H\alpha$  luminosity function (i.e. not corrected for dust) is shown in the plot in Fig. 5, where it is compared with the results obtained by Gilbank et al. (2010b). This shows that the MUSE sample is probing to significantly fainter luminosities than the SDSS sample of Gilbank et al. The latter sample was restricted to  $0.032 < z < 0.2$ . The SDSS spectra are reasonably well calibrated and the aperture corrections were made using the  $u$  band in the higher S/N SDSS Stripe 82 region. The offset evident in the figure is likely due to the underdensity (UD) of the MUSE sample discussed in Section 6.

For the GAMA sample, estimating  $H\alpha$  luminosity functions is significantly harder because of the smaller aperture used for the majority of spectra and the less accurate spectrophotometry (see Hopkins et al. 2013 for GAMA spectroscopic analysis). Gunawardhana et al. (2013) compute dust-corrected  $H\alpha$  luminosity functions for a similar GAMA sample and compare with other surveys as well. They discuss the problem of bivariate selection and the discrepancies between various results.

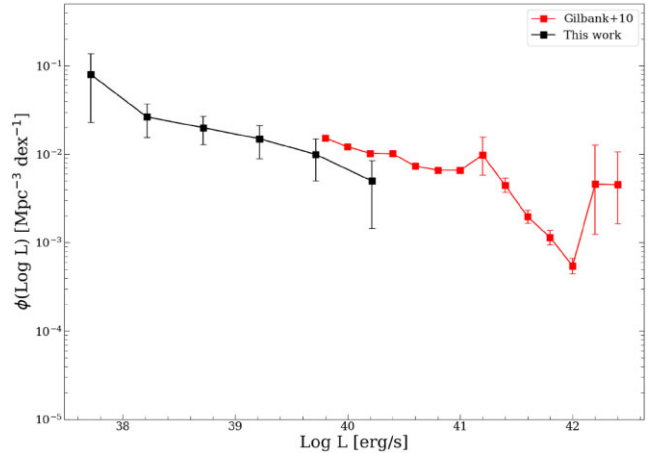


**Figure 5.** The observed  $H\alpha$  luminosity function derived using the combined sample from MUSE Wide and MUSE HUDF compared to Gilbank et al. (2010b). This demonstrates how this work focuses on the fainter end of the galaxy population. The luminosities used in this plot are not dust corrected.

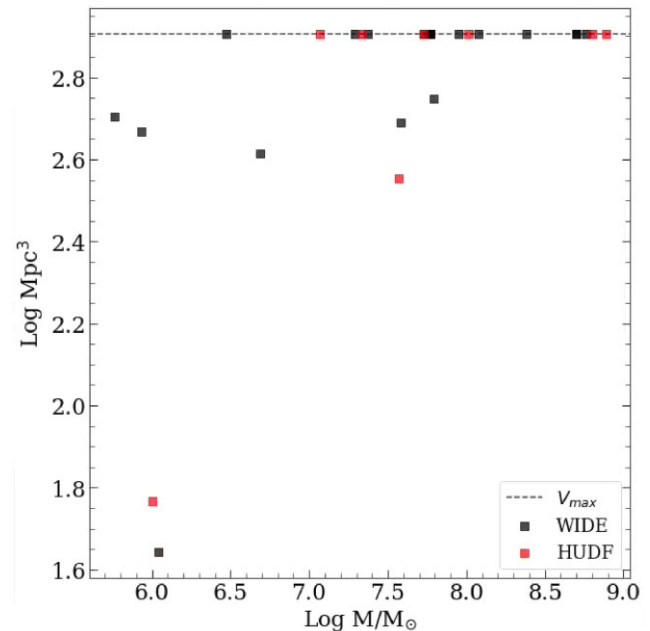


**Figure 6.** The maximum volume for each galaxy in the MUSE Wide and MUSE HUDF sample versus redshift. These are used for the estimation of the SFRD and luminosity function using the  $1/V_{\max}$  method.

## 5 RESULTS: THE SFRD AS A FUNCTION OF MASS

From the dust corrected  $H\alpha$  line fluxes measured by MUSE Wide and MUSE HUDF, the SFRs of the galaxies were calculated using the calibration shown in equation (1). Two star-forming galaxies, one from MUSE Wide and one from MUSE HUDF, although they have O III emission lines, do not present any confirmed  $H\alpha$  emission, so they were excluded from the analysis, resulting in a total of 27 sources (19 from Wide and 8 from HUDF). Before deriving the SFRD, the maximum volume of the survey was calculated using the detection limits determined previously. Fig. 6 shows the maximum volume of each galaxy, with  $V_{\max}$  derived considering the total volume of the two surveys combined, as described in Section 3.2. The plot

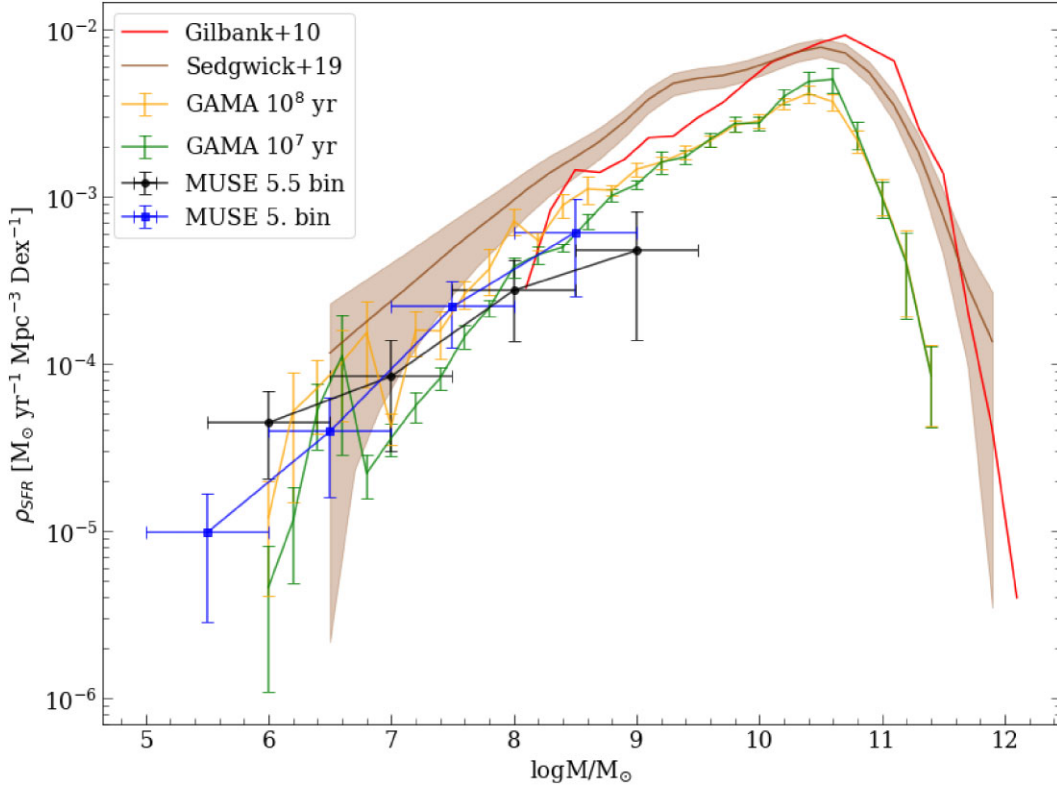


**Figure 7.** Comparison between SFRD estimates from this and previous work: the combined MUSE sample (using two different binning schemes); the GAMA sample (using two different MagPhys time-scales); the SDSS  $H\alpha$  Balmer decrement corrected measurement from Gilbank et al. (2010b); and the measurement using CCSNe from Sedgwick et al. (2019). The MUSE results use two different starting points,  $\log M/M_\odot = 5$  and  $\log M/M_\odot = 5.5$ , resulting in two overlapping functions.

shows that the galaxies with the lowest stellar masses tend to have lower  $V_{\max}$ , which is consistent with the expectation, as they tend to have lower  $H\alpha$  flux and thus, they would not be observed at further distances.

The SFRD for the combined MUSE Wide and MUSE HUDF sample was derived using the  $V_{\max}$  method with equation (4) described in Section 3.2. Given the limited number of galaxies in the sample, the mass bins were chosen to be relatively wide, with a value of  $\Delta \log M/M_\odot = 1$ . This was necessary in order to have a reasonable estimate of the uncertainty using weighted-Poisson errors for each bin (Bohm & Zech 2014; the variance is the sum of weights squared with the weights as per equation 4). The SFRD was calculated starting from two different mass bins,  $\log M/M_\odot = 5$  and  $\log M/M_\odot = 5.5$ , resulting in two overlapping functions for the same sample.

The SFRD was also calculated using a sample from the GAMA survey, a large magnitude-limited spectroscopic survey. Compared to MUSE Wide and MUSE HUDF, GAMA is shallower (and missing low surface brightness galaxies) but with a much larger area, comprising a vaster number of galaxies and thus also providing a good indication of the number density at lower stellar masses. The GAMA catalogue used contained measurements of spectroscopic redshifts from the SpecCat DMU, stellar masses from StellarMasses DMU, and SFR measurements at different time-scales derived through SED fitting with MagPhys in the MagPhys DMU. SED measurements of SFRs were used instead of deriving the SFR using measurements of  $H\alpha$  emission line flux measurements, as GAMA fibre spectroscopy may overestimate their values for dwarf galaxies (Richards et al. 2016). Since only young, massive stars with ages  $< 20$  Myr produce

$H\alpha$  emissions (Davies et al. 2016), the median SFR at time-scales of  $10^7$  and  $10^8$  were used in this analysis (from the MagPhys table). After ensuring that only galaxies with valid measurements were included, the final sample from GAMA consisted of 7579 galaxies at redshift  $z < 0.06$  from the equatorial regions that are highly complete ( $179 \text{ deg}^2$ ).

The results for the SFRD using the combined MUSE sample at different mass bins and using the GAMA sample at different time-scales can be seen in Fig. 7. The plot shows that the samples appear to concur, with a steady decline at the lower mass end of the SFRD( $M$ ). The decline may be quantified by assuming a linear regression between SFRD and stellar mass in log space at lower stellar masses, and measuring its slope  $\gamma$ , i.e.

$$\frac{d \text{SFRD}}{d \log M} \propto M^\gamma. \quad (12)$$

The linear fit was calculated using the standard least-squares fitting method, where the diagonal elements of the covariance matrix correspond to the variances of the slope and intercept. In our analysis, the resulting values of the slope in SFRD are  $\gamma = 0.57 \pm 0.16$  for the combined MUSE sample (note that for this value is derived using stellar mass bins of  $\Delta \log M/M_\odot = 0.5$ ),  $\gamma = 0.73 \pm 0.14$  for the GAMA sample with median SFR at time-scales of  $10^7$  yr, and  $\gamma = 0.65 \pm 0.11$  for the GAMA sample median SFR at time-scales of  $10^8$  yr. The SFRD for the GAMA sample were only fitted for  $M < 10^8 M_\odot$ .

The contribution of low-mass galaxies to the cosmic SFRD has been measured in this paper. The slope of the SFRD is related to the slope of the GSMF, which is commonly modelled using a Schechter

function so that the linear number density is proportional to  $M^\alpha$ , with  $\alpha$  representing the slope of the GSMF at the faint end. Hence, the number density per logarithmic mass bin is given by

$$\frac{dN}{d \log M} \propto M^{\alpha+1}. \quad (13)$$

Considering the relation between SFR and stellar mass of star-forming galaxies, the SFR of a galaxy is approximately proportional to its stellar mass so that

$$\text{SFR} \propto M^\beta, \quad (14)$$

with  $\beta \sim 1$ , at masses below about  $10^{10} M_\odot$ , along the star-forming main sequence (Brinchmann et al. 2004; Lee et al. 2015; McGaugh, Schombert & Lelli 2017). Since the SFRD is the number density times the mean SFR (e.g. Behroozi, Wechsler & Conroy 2013), the relationship between the slopes of the SFRD, SFR-mass relation and GSMF (of star-forming galaxies) can be expressed as

$$\gamma = \alpha + \beta + 1. \quad (15)$$

This is accurate over any mass range where there is no significant break in the power laws.

It is possible to estimate the GSMF directly from these samples, however, they are expected to be incomplete even for star-forming galaxies at low masses. This especially true for  $H\alpha$  selection which is highly biased towards high SFR galaxies, with significantly reduced detectability for low SFRs (lower luminosity, equivalent width and surface brightness). Instead if we assume  $\beta \simeq 1$  along the main sequence of star-forming galaxies, the above relationship (equation 15) becomes  $\alpha \simeq \gamma - 2$ . Therefore, the values of the slope of the SFRD imply  $\alpha$  in the range  $-1.5$  to  $-1.2$ . These values are consistent with previous studies of the GSMF (Moustakas et al. 2013; Wright et al. 2017; Thorne et al. 2021; Driver et al. 2022), providing further evidence of no turn-over at lower masses.

## 6 DISCUSSION

The SFRD results from the combined sample using the MUSE Wide and MUSE HUDF catalogues, and the results obtained using the catalogues from the GAMA survey, show the behaviour of the SFRD down to stellar masses of  $\sim 10^{5.5} M_\odot$  with MUSE and  $\sim 10^6 M_\odot$  with GAMA, pushing our understanding of the SFRD to the faintest galaxies. The results from this work indicate that low-mass galaxies ( $\sim 10^{6.5} M_\odot$ ) contribute about 1 percent of the cosmic SFRD (per dex) relative to massive galaxies at the peak of the SFRD( $M$ ).

The MUSE sample benefited from accurate  $H\alpha$  emission line flux measurements, thanks to MUSE Wide and MUSE HUDF advanced IFU spectroscopy; therefore, the SFR for this sample was derived using the calibration described in Section 3.1. However, since the sample only contained a limited number of 27 galaxies, the SFRD could only be derived using large stellar mass bins of  $\Delta \log M/M_\odot = 1$ , in order to ensure a reasonable Poisson error. None the less, the results show reasonable agreement with the extrapolation based on previous studies, and with the SFRD estimated using GAMA.

The SFRs used for the analysis of the GAMA sample were derived via SED fitting using MagPhys (da Cunha et al. 2008), as the  $H\alpha$  emission line measurements for low-mass galaxies in GAMA might be inflated and too susceptible to corrections required for aperture effects. However, its large area allowed us to create a sample of 7579 star-forming galaxies at  $z < 0.06$ . As shown in Fig. 7, the slope of the GAMA SFRD is similar to the one found using MUSE at low masses. There is an increase in the SFRD derived from GAMA as stellar mass increases up to  $\sim 10^{10.5} M_\odot$ . There is a sharp decline at

the higher end of the function as expected from the exponential cutoff in the GSMF and from the higher fraction of quenched galaxies at higher masses.

Previous studies encountered difficulties in estimating the SFRD below  $\sim 10^8 M_\odot$ , as dwarf galaxies are challenging to observe. Gilbank et al. (2010b) derived the SFRD down to stellar masses of  $\sim 10^8 M_\odot$  using  $H\alpha$ , [O II], and  $u$ -band luminosities from the SDSS, whereas Sedgwick et al. (2019) managed to estimate the SFRD at  $\sim 10^7 M_\odot$  using CCSNe as ‘signposts’ to low surface brightness galaxies to constrain their abundance and contribution to the total SFRD at lower masses. As shown in Fig. 7, both studies suggested a constant decline in SFRD, similarly to the results found in this work.

The SFRD measurements of Sedgwick et al. (2019) and Gilbank et al. (2010b) do appear offset from our work. However, Sedgwick et al. used a factor of two correction at low galaxy masses for the visibility of CCSNe, and there is uncertainty over classification of CCSNe for some of their sample. This also requires a CCSNe rate to SFRD calibration. So this SFRD from CCSNe may be overestimated. Gilbank et al. used a different calibration of  $H\alpha$  luminosity to SFR (from Kennicutt 1998). This SFRD is shown adjusted to our calibration ( $\times 0.7$ ) in Fig. 8.

A constant decline in SFRD at lower stellar masses could have great significance in our understanding of the GSMF and galaxy evolution. In fact, the results ( $\gamma < 1$ ) suggest that there is no turn-over at the faint end of the GSMF down to  $\sim 10^6 M_\odot$ . This is based on the assumption that the main-sequence slope (equation 14) is approximately unity (e.g. Lee et al. 2015). Or in other words, the mean specific SFR of star-forming galaxies is similar for mass ranges below  $10^{10} M_\odot$  (James et al. 2008b). This is expected if these galaxies have formed their stars quasi-continuously since galaxy formation began.

A reasonable estimate of the SFRD does not require that we find all star-forming galaxies in a given volume. It is plausible that low-mass star-forming galaxies may go through lull periods (but not quenched) which would reduce their  $H\alpha$  luminosity significantly and thus not appear in  $H\alpha$ -selected samples. This is the duty cycle of star formation and it is likely more extreme at low masses. In effect, the SFRD over a cosmological volume is an estimate of the time average over a population of star-forming galaxies. This is because we do not expect the chance of being in a lull or burst phase being correlated with other star-forming dwarf galaxies.

The implications of our findings highlights the importance of low-mass galaxies in various cosmological processes. The slope of the SFRD suggests a steep faint-end slope for the GSMF, consistent with prior studies (e.g. Wright et al. 2017). This highlights the importance of low-mass galaxies in the star formation budget and their potential role in early cosmic epochs.

The volume of the MUSE sample is only  $804 \text{ Mpc}^3$ . Therefore, this is potentially subject to significant cosmic variance. To test this, we consider previous observations of the GSMF from the GAMA survey (Baldry et al. 2012; Wright et al. 2017). Measurements of the number density for galaxies more massive than  $10^8 M_\odot$  are not affected by low surface brightness incompleteness in GAMA. Integrating the number density from the high-mass end, we obtain between 0.028 and 0.036 galaxies per  $\text{Mpc}^3$  by changing the log-mass limit between 7.9 and 8.1. This allows for some uncertainty in how stellar mass is estimated.

As the volume of the combined MUSE sample is  $804 \text{ Mpc}^3$ , the expected number of galaxies with stellar masses higher than  $10^8 M_\odot$  should be between 22 and 29. However, the total number of galaxies above this mass limit, including passive (non-star-forming) galaxies detected using AUTOZ (Baldry et al. 2014), in the volume of interest

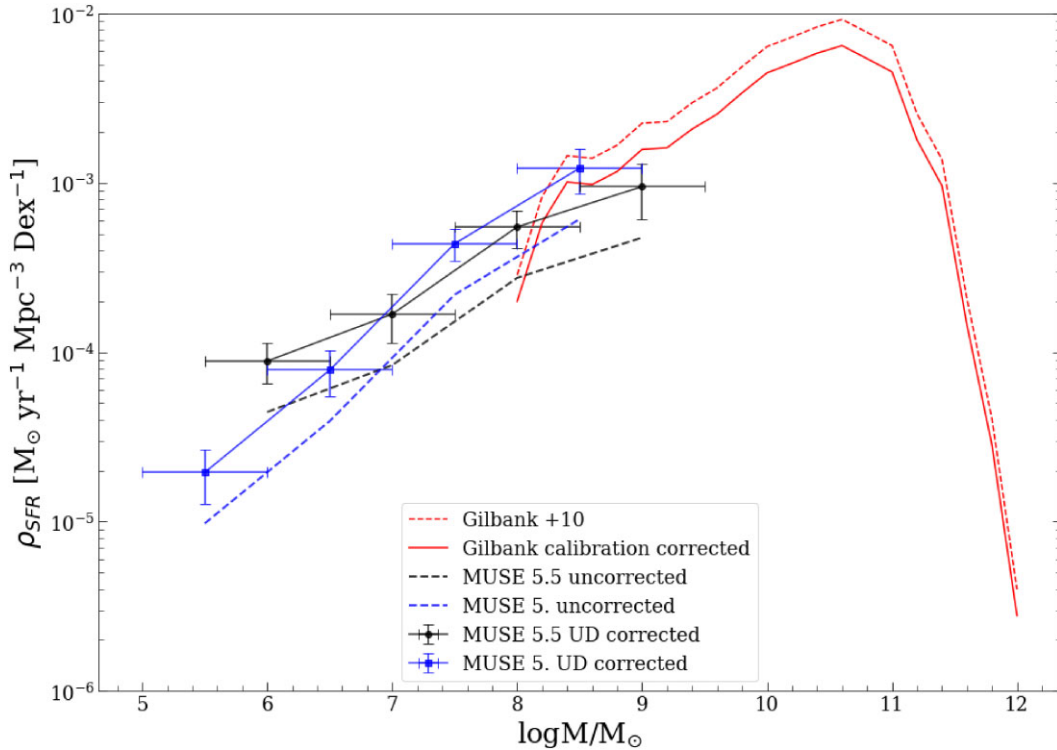


**Figure 8.** SFRD with respect to stellar mass using  $H\alpha$  line emission. The MUSE combined sample is shown with and without a correction for the estimated UD of the sample. The uncorrected and UD corrected results are both shown for two different binning schemes starting at 5.0 and 5.5 in log mass. The Gilbank et al. (2010b) result is shown with and without a correction to convert their SFR– $H\alpha$  calibration to that of equation (1).

is only 12. These results suggest that the volume is underdense. If we assume that the number density of galaxies below  $10^8 M_\odot$  scales in the same way, we can account for the UD by multiplying the values of the SFRD by about 2.

This simple correction can be seen in the plot reported in Fig. 8, where it can be seen how by accounting for UD, the SFRD is more consistent with the values derived in previous studies (Gilbank et al. 2010b; Sedgwick et al. 2019). These results suggest that a larger sample is required to have a conclusive understanding of the low-mass galaxy population and their impact on the SFRD and GSMF. These results may also provide a useful benchmark for comparisons with future deep field surveys and cosmological simulations.

## 7 SUMMARY

This study investigates the contribution of star-forming galaxies to the SFRD as a function of stellar mass at  $z < 0.2$ , using MUSE Wide, MUSE HUDF, and GAMA surveys. By combining deep spectroscopic coverage and wide-area data, we probe the faint end of the SFRD down to stellar masses of  $10^{5.5} M_\odot$ , providing new insights into the low-mass galaxy population. In summary, the results from this work show that:

(i) The MUSE Wide and MUSE HUDF surveys have a total volume of  $804 \text{ Mpc}^3$ . Their exceptional depth allowed us to detect 27 star-forming galaxies with  $H\alpha$  emission lines at redshifts  $z < 0.2$ . On the other hand, the sample from the GAMA survey benefited from a much larger number of galaxies, with a total of 7579 galaxies at redshift  $z < 0.06$ . For GAMA, we rely on the photometric estimates of the SFRs from SED fitting because the spectroscopic  $H\alpha$  measurements require significant aperture corrections.

(ii) The  $H\alpha$  luminosity function reported in Fig. 5 was derived using a combined sample of galaxies from MUSE Wide and MUSE HUDF down to values of  $\sim 10^{38} \text{ erg s}^{-1}$ . This shows that we push to significantly lower luminosities in  $H\alpha$  compared to those used for the SFRD measurements of Gilbank et al. (2010b).

(iii) The SFRD with respect to stellar mass distribution was estimated for the MUSE Wide and HUDF combined sample, using SFR  $H\alpha$  measurements, and the GAMA sample, using SFRs values derived with MagPhys SED fitting. The results shown in Fig. 7 suggest that there is a constant slope in SFRD at lower masses with values of the slope  $\gamma$  (equation 12) between 0.57 and 0.73. This quantifies the contribution of low-mass galaxies to the cosmic SFRD.

(iv) The slope in SFRD( $M$ ) implies that the faint-end slope in the GSMF,  $\alpha$ , is in the range  $-1.5$  to  $-1.2$  (see equations 13–15 for this argument), consistent with values found in GAMA (Baldry et al. 2012; Wright et al. 2017), providing important evidence of the absence of a turn-over at the faint end of the GSMF.

(v) When considering the number density of galaxies more massive than  $10^8 M_\odot$  using the GAMA GSMFs compared with the number of galaxies detected at  $z < 0.2$  in MUSE Wide and MUSE HUDF, there is a significant discrepancy between the number densities. This implies that the volume considered in MUSE is underdense, with about a factor of two fewer galaxies than the cosmic mean.

(vi) The results could be improved with larger surveys, allowing us to more accurately investigate the faint end of the SFRD and GSMF, and with comparisons with cosmological simulations. For example, the Rubin Observatory can be used to detect and characterize the SFRD using CCSNe; while *Euclid* imaging (to detect low surface brightness galaxies) plus redshifts from 4MOST provide a deeper

galaxy redshift survey. And we could also use more MUSE fields (blind to low-redshift volume) for H $\alpha$  selected galaxy samples.

## ACKNOWLEDGEMENTS

We thank the anonymous referee for thoughtful comments that significantly improved the paper. We would like to express our sincere gratitude to Prof. Phil James for his invaluable guidance and support throughout this work. We also thank the MUSE collaboration for providing the data used in this research, particularly from the MUSE Wide and MUSE HUDF surveys. Finally, GM acknowledges the financial support from the Science and Technology Facilities Council (STFC) for funding his PhD.

## DATA AVAILABILITY

The data underlying this article are all publicly available. The MUSE Wide survey data can be accessed from <https://musewide.aip.de/>, and the MUSE HUDF DR2 survey data are available at <https://amused.univ-lyon1.fr/>. Additionally, the data from the GAMA survey are accessible from <https://www.gama-survey.org/dr4/>.

## REFERENCES

- Bacon R. et al., 2010, in McLean I. S., Ramsay S. K., Takami H., eds, Proc. SPIE Conf. Ser. Vol. 7735, Ground-based and Airborne Instrumentation for Astronomy III. SPIE, Bellingham, p. 773508
- Bacon R. et al., 2015, *A&A*, 575, A75
- Bacon R. et al., 2017, *A&A*, 608, A1
- Bacon R. et al., 2023, *A&A*, 670, A4
- Baldry I. K. et al., 2012, *MNRAS*, 421, 621
- Baldry I. K. et al., 2014, *MNRAS*, 441, 2440
- Baldry I. K. et al., 2018, *MNRAS*, 474, 3875
- Beeston R. A. et al., 2018, *MNRAS*, 479, 1077
- Behroozi P. S., Wechsler R. H., Conroy C., 2013, *ApJ*, 770, 57
- Blanton M. R. et al., 2003, *AJ*, 125, 2348
- Bohm G., Zech G., 2014, *Nucl. Instrum. Methods Phys. Res. A*, 748, 1
- Bouwens R. J. et al., 2015, *ApJ*, 803, 34
- Brinchmann J., Charlot S., White S. D., Tremonti C., Kauffmann G., Heckman T., Brinkmann J., 2004, *MNRAS*, 351, 1151
- Budavári T. et al., 2009, *ApJ*, 694, 1281
- Calzetti D., 2013, in Falcón-Barroso J., Knapen J. H., eds, Secular Evolution of Galaxies. Cambridge Univ. Press, Cambridge, p. 419
- Calzetti D., Armus L., Bohlin R. C., Kinney A. L., Koornneef J., Storchi-Bergmann T., 2000, *ApJ*, 533, 682
- Cardelli J. A., Clayton G. C., Mathis J. S., 1989, *ApJ*, 345, 245
- Cross N., Driver S. P., 2002, *MNRAS*, 329, 579
- da Cunha E., Charlot S., Elbaz D., 2008, *MNRAS*, 388, 1595
- da Cunha E. et al., 2015, *ApJ*, 806, 110
- Davies L. J. et al., 2016, *MNRAS*, 461, 458
- Domínguez A. et al., 2013, *ApJ*, 763, 145
- Drake A. B. et al., 2015, *MNRAS*, 454, 2015
- Driver S. P. et al., 2018, *MNRAS*, 475, 2891
- Driver S. P. et al., 2022, *MNRAS*, 513, 439
- Felten J., 1976, *ApJ*, 207, 700
- Garn T., Best P. N., 2010, *MNRAS*, 409, 421
- Giavalisco M. et al., 2004, *ApJ*, 600, L93
- Gilbank D. G. et al., 2010a, *MNRAS*, 405, 2419
- Gilbank D. G., Baldry I. K., Balogh M. L., Glazebrook K., Bower R. G., 2010b, *MNRAS*, 405, 2594
- Gordon Y. A. et al., 2016, *MNRAS*, 465, 2671
- Grogin N. A. et al., 2011, *ApJS*, 197, 35
- Groves B., Brinchmann J., Walcher C. J., 2012, *MNRAS*, 419, 1402
- Gunawardhana M. L. P. et al., 2013, *MNRAS*, 433, 2764
- Herenz E. C., Wisotzki L., 2017, *A&A*, 602, A111
- Herenz E. C. et al., 2017, *A&A*, 606, A12
- Hopkins A. M., Beacom J. F., 2006, *ApJ*, 651, 142
- Hopkins A. M. et al., 2013, *MNRAS*, 430, 2047
- James P. A., Knapen J., Shane N., Baldry I., De Jong R., 2008a, *A&A*, 482, 507
- James P. A., Prescott M., Baldry I. K., 2008b, *A&A*, 484, 703
- Johnson B. D., Leja J., Conroy C., Speagle J. S., 2021, *ApJS*, 254, 22
- Kauffmann G. et al., 2003, *MNRAS*, 346, 1055
- Kennicutt R. C., 1998, *ApJ*, 498, 541
- Khostovan A. A., Malhotra S., Rhoads J. E., Sobral D., Harish S., Tilvi V., Coughlin A., Rezaee S., 2024, *MNRAS*, 535, 2903
- Koekemoer A. M. et al., 2011, *ApJS*, 197, 36
- Koyama Y. et al., 2015, *MNRAS*, 453, 879
- Kriek M. et al., 2018, Astrophysics Source Code Library, record ascl:1803.008
- Kroupa P., 2001, *MNRAS*, 322, 231
- Lee N. et al., 2015, *ApJ*, 801, 80
- Leja J., Speagle J. S., Johnson B. D., Conroy C., Van Dokkum P., Franx M., 2020, *ApJ*, 893, 111
- Lilly S. J., Le Fevre O., Hammer F., Crampton D., 1996, *ApJ*, 460, L1
- Liske J. et al., 2015, *MNRAS*, 452, 2087
- McGaugh S. S., Schombert J. M., Lelli F., 2017, *ApJ*, 851, 22
- Madau P., Dickinson M., 2014, *ARA&A*, 52, 415
- Madau P., Ferguson H. C., Dickinson M. E., Giavalisco M., Steidel C. C., Fruchter A., 1996, *MNRAS*, 283, 1388
- Mary D., Bacon R., Conseil S., Piqueras L., Schutz A., 2020, *A&A*, 635, A194
- Moustakas J. et al., 2013, *ApJ*, 767, 50
- Osterbrock D. E., Ferland G. J., 2006, Astrophysics of Gas Nebulae and Active Galactic Nuclei. University Science Books, Sausalito, CA
- Rafelski M. et al., 2015, *AJ*, 150, 31
- Richards S. N. et al., 2016, *MNRAS*, 455, 2826
- Schaye J. et al., 2010, *MNRAS*, 402, 1536
- Schmidt M., 1968, *ApJ*, 151, 393
- Schulze S. et al., 2021, *ApJS*, 255, 29
- Sedgwick T. M., Baldry I. K., James P. A., Kelvin L. S., 2019, *MNRAS*, 484, 5278
- Skelton R. E. et al., 2014, *ApJS*, 214, 24
- Taylor E. N. et al., 2011, *MNRAS*, 418, 1587
- Thorne J. E. et al., 2021, *MNRAS*, 505, 540
- Tremonti C. A. et al., 2004, *ApJ*, 613, 898
- Tresse L., Maddox S. J., 1998, *ApJ*, 495, 691
- Urrutia T. et al., 2019, *A&A*, 624, A141
- van der Wel A. et al., 2014, *ApJ*, 788, 28
- van Zee L., 2001, *AJ*, 121, 2003
- Wright A. et al., 2017, *MNRAS*, 470, 283
- York D. G. et al., 2000, *AJ*, 120, 1579

This paper has been typeset from a  $\text{\TeX}/\text{\LaTeX}$  file prepared by the author.